Philosophical Magazine,
Vol. 85, No. 19, 1 July 2005, 2147–2175

3D quantitative image analysis of open-cell nickel foams under tension and compression loading using X-ray microtomography

T. DILLARD†, F. N'GUYEN†, E. MAIRE‡, L. SALVO§, S. FOREST*†, Y. BIENVENU†, J.-D. BARTOUT†, M. CROSET¶, R. DENDIEVEL§ and P. CLOETENS‖

†Ecole des Mines de Paris, Centre National de la Recherche Scientifique, Centre des Matériaux, UMR 7633, BP 87, 91003 Evry, France
‡INSA de Lyon, CNRS, Group d'Etude de Métallurgie Physique, UMR 5510, 20 Av. A. Einstein, 69621 Villeurbanne, France
§INP de Grenoble, CNRS, Génie Physique et Mécanique des Matériaux, UMR 5010, Domaine Universitaire, BP 46, 38402 Saint Martin d'Hères, France
¶Technologies Conseil, 48 rue du Moulin, 91120 Palaiseau, France
‖European Synchrotron Radiation Facility, BP 220, 38043 Grenoble, France

(*Received 25 March 2004; in final form 22 October 2004*)

The deformation behaviour and fracture of an open-cell nickel foam were analysed using X-ray microtomography at the ESRF, Grenoble, France. *In situ* tensile and compression tests were performed at a resolution of 2 and 10 μm. The initial morphology of the foam was studied using 3D image analysis. Parameters such as the cell volume and strut length distributions, number of faces per cell, number of nodes per face and the shape of the most representative cells were determined. The cells are shown to be non-spherical due to the initial geometrical anisotropy of the polyurethane foam template and to the load applied to the nickel foam during processing. This geometrical anisotropy is shown to be related to the observed anisotropy of the elastic properties of the material using a simple beam model. In tension, bending, stretching and alignment of struts are observed. A tensile test in the longitudinal direction is shown to reinforce the privileged orientations of the cells. In contrast, a tensile test in the transverse direction leads to a more isotropic distribution of the cells. These features are illustrated by pole figures of the three axes of equivalent ellipsoids for all cells at different strain levels. Compression tests are associated with strain localization phenomena due to the buckling of struts in a weaker region of the foam. Finally, study of open-cell nickel foam fracture shows that cracks initiate at nodes during tensile tests and that the damaged zone is about five cells wide. Free edge effects on crack initiation are also evidenced.

1. Introduction

Open-cell nickel foams are widely used for electrodes in battery applications. They play the role of container for the electrolyte and collector of electric current.

*Corresponding author. Email: samuel.forest@ensmp.fr

Philosophical Magazine
ISSN 1478–6435 print/ISSN 1478–6443 online © 2005 Taylor & Francis Group Ltd
http://www.tandf.co.uk/journals
DOI: 10.1080/14786430412331331916

During the processing of the battery component, the foams are also subjected to severe mechanical loading conditions. This requires outstanding mechanical properties of the foams in tension and compression. There is a strong endeavour to relate these mechanical properties to the explicit morphology of the cells. The cell morphology of open-cell nickel foams is the result of two contributions: the cell morphology of the initial polymer foam template and its evolution during the manufacturing process.

Recent observations using X-ray microtomography demonstrated that this technique is suitable for the investigation of the 3D structure and deformation of metallic foams [1–5]. However, systematic statistical analyses of the morphology of cells in open-cell metal foams, especially its evolution during straining, remain scarce [6–8]. The present work reports the analysis of *in situ* tensile and compression tests performed on open-cell nickel foams at the ESRF, Grenoble. The aim of this study is to provide quantitative information on the morphology of open-cell nickel foams regarding the shape and size of the most representative cells and the corresponding statistics. The evolution of these characteristics during tension and compression loading is described in detail. Attention is focused on the anisotropy of the observed cells and its evolution during straining. Another issue is to relate this aspect ratio to the observed anisotropic mechanical properties of the considered foam. Finally, X-ray microtomography is also a tool well-suited to explore the damage and failure mechanisms arising in the last deformation stages.

For that purpose, 3D image analysis procedures are necessary, for instance to close and segment the cells. A simple threshold technique as used for closed-cell foams is not possible [9–12]. A systematic 3D segmentation method for open-cell foams was presented in Dillard *et al.* [13] and will only be briefly recalled in this work. Further image analysis tools are then necessary to extract morphometric parameters such as the number of faces per cell, cell size and strut length distributions, equivalent ellipsoid dimensions and orientation.

A description of the specific processing of the considered nickel foam developed by the firm NiTECH, and presentation of the X-ray microtomography and mechanical testing procedures are given in section 2. Section 3 deals with the image analysis techniques used to derive the skeleton and associated graph of the observed samples. The results presented in section 4 provide an accurate statistical description of the initial cell morphology of the investigated samples and its evolution during two tensile and one compression tests. In the discussion of section 5, the typical cell shapes found are compared with previous results from the literature. The discussion also investigates the links between the observed geometrical anisotropy of the cells and the elastic anisotropy found for this material. For that purpose, a simple mechanical model in the spirit of Gibson and Ashby [14] is used. The evolution of the aspect ratio during tensile loading is discussed in subsection 5.3. The last subsection concentrates on the damage and fracture mechanisms at work in the nickel foam.

2. Experimental methods

2.1. *Material processing*

Three processing routes are possible for stochastic open-cell metal foams [15]: liquid, via casting into a mold; solid, via coating of a polymer template; and vapour phase,

via chemical or physical vapour deposition. Most of these manufacturing methods start from an open-cell polymer foam template. The specific process developed by the firm NiTECH for nickel foams uses vapour deposition [16]. It can be divided into five main steps. Firstly, a polyurethane foam plate with the desired thickness and porosity for the final product is selected as a foam template. The polymer foam used in this work is 1.6 mm thick and is delivered as coils of 1.2 m width. The thickness of our samples cannot be larger than that of the coil from which they are cut, so all the samples tested in the present study are 1.6 mm thick. The impact of this small thickness on the representativeness of the obtained results is discussed later in the paper. Cathodic magnetron nickel sputtering is then used to cover the foam template with a thin layer of nickel. This 0.1 μm thick nickel deposit is sufficient to make the foam electrically conductive. An electroplating technique is then used for the deposition of a 10 μm thick nickel layer. The polymer template is burnt and a final heat treatment is carried out to improve the ductility of the foam. A slight tensile load is applied during the whole continuous process. Finally, nickel foams are packaged and sold in the form of coils.

In this work, the tensile direction of the process is called RD. It coincides with the main length of the final coils. The transverse and normal directions are denoted respectively by TD and ND.

The relative density of nickel foams is defined as the ratio of the mass density of the cellular material to that of pure nickel. In this work, the relative density of the studied nickel foams is

$$\rho^* = \frac{\rho_{\text{foam}}}{\rho_{\text{Ni}}} = 0.035, \quad \text{with } \rho_{\text{Ni}} = 8908\,\text{kg}\,\text{m}^{-3} \tag{1}$$

Other aspects of the material processing directly influence the cell morphology of the foam and its mechanical behaviour. For instance, struts are hollow, due to burn out of the polymer foam template. A thickness gradient of the nickel layer in the foam is also introduced by the electroplating technique. The thickness t_e of the nickel layer deposited at the external surface of the foam is larger than the thickness t_i in the internal mid-section. A thickness deposit ratio (TDR) can thus be defined for the foam:

$$\text{TDR} = \frac{t_e}{t_i} \tag{2}$$

Its value, determined by 2D image analysis, is found to be equal to 1.5 for the material studied in this work.

2.2. *X-ray microtomography*

High-resolution tomographic experiments were performed using a synchrotron X-ray source on beam line ID19 at the European Synchrotron Radiation Facility (ESRF), Grenoble. This line delivers a very intense monochromatic beam which allows images of a high signal-to-noise ratio to be acquired. The sample is fixed on a rotation stage between the X-ray source and the detection unit that records the transmitted X-rays. A fluorescent screen, coupled to a low-noise 1024 × 1024 pixel CCD camera (Fast REadout LOw Noise), is used to detect the projections of

the parallel beam. Finally, the resulting images of these projections are retrieved in grey-level tone. The contrast in these images depends on the linear attenuation coefficient μ. The higher the atomic number Z and the material density ρ for a given photon energy E, the higher the linear attenuation coefficient.

A tensile/compression machine has been added to the experimental set-up. It is described in section 2.3. The whole tensile/compression rig is fixed on the ESRF precise translation–rotation stage. Once the sample is placed on the loading rig, a 2D radiograph is acquired. Then, the whole machine is rotated under the beam incrementally up to 180° to provide a set of 900 radiographs. These radiographs are used by reconstruction software to give a 3D numerical image of the studied material. A complete scan consists of 900 radiographs and about 100 reference images of the background. Intensity inhomogeneities and variations of the X-ray beam can be eliminated by subtraction of the reference images. The high photon flux delivered by the ESRF allows reduction of the exposure time to 1 s per radiograph. The acquisition of a complete scan lasts approximately 15 min.

The beam energy was set to 30 keV and two resolutions (2 and 10 μm) were chosen according to the strut thickness and the mean cell diameter of the studied material. Indeed, the 10 μm resolution gives statistical data at the cell scale, whereas the 2 μm resolution provides detailed observations, on damage for instance, at the strut scale. This choice of the resolution dictates the sample width. The largest dimension of the sample is kept smaller than the field of the detector (e.g. 10.24 mm for a 10 μm resolution), because the complete material has to be illuminated by the beam at each rotation [17–19].

2.3. *In situ mechanical testing*

A tensile/compression machine was especially designed to allow the observation of deformation and damage by X-ray microtomography [20]. To allow the X-ray beam to go through the machine while transmitting the load between the upper mobile grip and the lower fixed grip, a transparent polymer tube is used in the central part of the machine. This tube has been carefully polished and gives negligible and constant attenuation on every 2D radiograph. A 2 kN cell load is set on the lower grip. An extensometer is fixed on the upper grip. The upper grip is translated using an endless screw. Force and displacement are recorded on a computer. Tests are displacement controlled.

A specific device has been developed for the tensile tests in the present study. First, the sample's ends are glued between aluminium plates. The advantages of these plates consist of having a perfectly plane and large contact area between the plate and the grip, and also in automatically aligning the sample with respect to the loading axis. Samples are handled carefully to avoid any twist or bending because of the weight of the plates. Once the sample is set in the machine, a first scan is acquired to characterize the initial state. Then, the tensile test begins. Once the chosen displacement value is reached, it is kept constant for scanning the current state of the foam. Then the displacement is increased, and so on.

For compression tests, the sample is placed between two parallel plates. The upper grip is moved down until a small variation of the force is detected.

Then, the compression test begins. The test is interrupted for scanning the current state of the foam. For each tensile and compression test, five scans are performed at different strain levels. The compression loading direction is parallel to the direction ND.

Tensile specimens have a dog-bone shape to restrict the studied area (see figure 1). Their sizes are, respectively, 15 mm height, 5 mm width and 1.68 mm thickness for the 10 μm resolution, and 4.7 mm height, 1.2 mm width, and 1.68 mm thickness for the 2 μm resolution. Due to their small width, specimens were cut by an electro-discharge machining wire. Tensile specimens are cut along directions RD and TD in order to evidence the anisotropic behaviour of the foam. For compression tests, the sample is rectangular with 6.8 mm length, 4.3 mm width and 1.68 mm thickness for the 10 μm resolution. Due to the dimensions of the tensile specimens, two scans are necessary to follow the whole area of interest along the gauge length at each deformation stage, whereas only one scan is needed in compression.

3. 3D image analysis

The 3D segmentation of the cells of open-cell foams by means of 3D image analysis is a difficult task. To compute morphometric parameters, each cell of the foam first has to be isolated. Some criteria must be determined to reconstruct the cell walls. Such a systematic 3D segmentation method has been proposed recently in Dillard *et al*. [13]. The procedure and the results of the 3D segmentation are recalled here.

3.1. *3D segmentation procedure*

Due to the large difference between the linear attenuation coefficients of air and nickel, the grey-level distribution of the images is almost bimodal. A simple thresholding operation is applied to generate binary images. Then, the hollow struts are filled in by straightforward morphological operations.

The 3D segmentation method is divided into three main steps. First, the distance map image of the cells is computed and the position of the ultimate eroded sets, called markers, is determined [21, 22]. The right markers are then selected by topographic conditions. Finally, the watershed is constructed from these markers with the help of the distance function [23]. The result is that open cells can be closed and isolated in 3D [23]. A 2D section of the foam and the segmented image are shown in figure 2. This segmentation allows us to directly determine the value of some morphometric parameters, such as the volume of each cell. However, other morphometric parameters require knowledge of the 3D skeleton (one voxel thick) of the foam. For that purpose, the resulting 3D watershed, which is one or two voxels thick, is made thinner to attain a thickness of one single voxel.

3.2. *3D skeleton and graph of open-cell foams*

To obtain the 3D skeleton and the graph of the structure, the following procedure has been developed. The graph of open-cell foams is a node–strut representation and consists of lists of node coordinates and the node connectivity for the entire foam. First, a label is assigned to each closed cell of the foam. Then, the neighbourhood

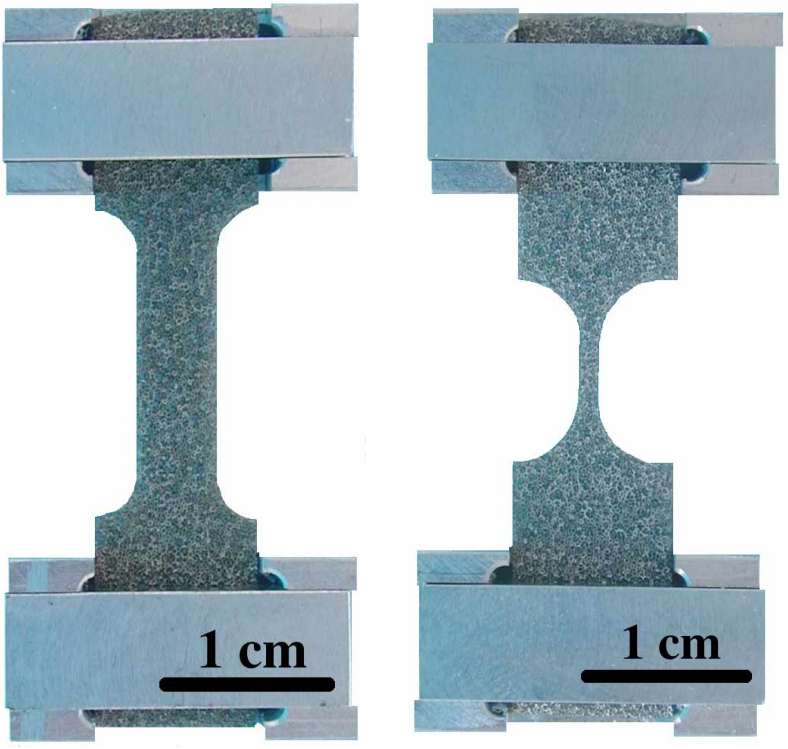

(a) (b)

Figure 1. Specimens for *in situ* tensile tests: (a) sample for 10 μm resolution, (b) sample for 2 μm resolution.

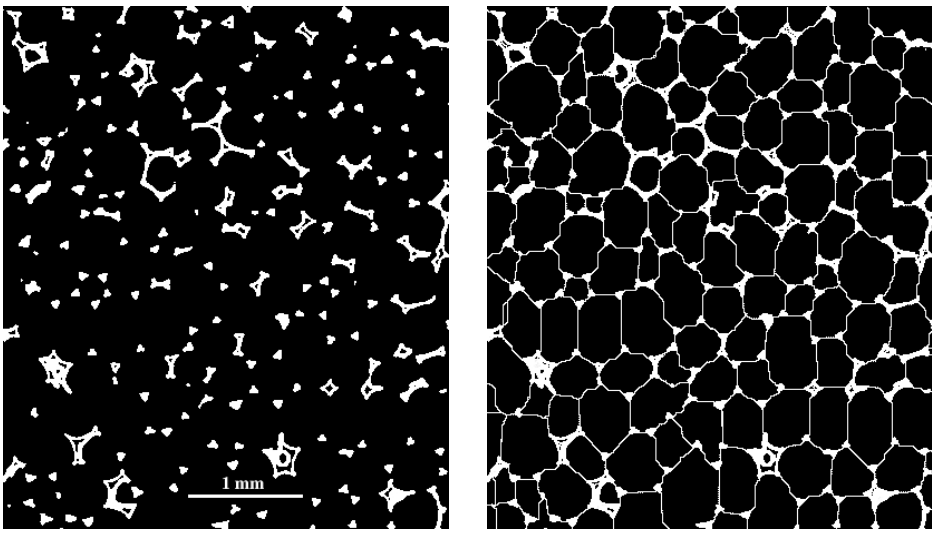

(a) (b)

Figure 2. 3D segmentation of open-cell foams: (a) 2D section of the foam, (b) corresponding section of the 3D closed cells.

($3 \times 3 \times 3$) of each voxel of the watershed is studied. The label of the most represented cell in the neighbourhood is assigned to each voxel of the watershed. As a result, each voxel of the image belongs to one specific cell. Finally, the derivative of the labels is computed to obtain the 3D skeleton.

This 3D skeleton contains the edges, and also the walls, of the closed cells. To retrieve the open-cell structure, the voxels of the skeleton are selected according to Plateau's laws [24]. From area minimizing principles, Plateau indicated that edges are formed by three liquid films equally inclined toward one another, with mutual angles equal to 120°, and that vertices are formed by four edges equally inclined toward one another. Thus, three cells should meet along edges, and four cells should meet at vertices. Voxels of the skeleton that have only two labels in their neighbourhood are considered as faces, three labels as struts and four or more labels as nodes. Only nodes and struts are kept in the final image. The resulting graph of the open-cell nickel foam structure is given in figure 3.

4. Results

4.1. *Initial cell morphology*

The initial state of the foam was studied to provide an accurate description of its morphology. Indeed, a knowledge of foam morphology can influence the choice of the representative unit cell to model the mechanical behaviour of foams [25, 26]. To obtain a statistically representative result, a large initial volume is analysed. It is 4.7 mm long, 4 mm wide, 1.68 mm thick, and contains 143 cells. Incomplete cells at the boundary are excluded from the analysis, unless otherwise stated.

4.1.1. Cell volume distribution. The volume of the individual cells is the first parameter that can be computed easily once the cells have been segmented. The volume of each cell is determined by counting the voxels belonging to the cell. A marching cube algorithm is used to better estimate this parameter [27]. Figure 4a shows the cell volume distribution. The distribution is mono-modal, centred around 0.07 mm^3, with a peak at 0.08 mm^3. The average cell volume is 0.071 mm^3. If the cells were spherical, the diameter of the mean cell would be equal to 514 μm.

4.1.2. Node coordination. Voxels with four labels or more in their neighbourhood are considered as nodes (see section 3.2). According to Plateau's rules, each junction of the foam belongs to a tetrahedron. Each junction is composed of four edges with an angle of 109°. The node coordination must be four for each node. The node coordination distribution in the graph of the studied foam is given in table 1. As expected, the node coordination distribution appears well-centred around 4 with a sharp maximum. More than 70% of the nodes are the intersection of four struts. Another peak is detected for the value 1. This peak comes from nodes placed at the boundary of the node–strut representation. The analysis of node coordination was performed without excluding the struts of incomplete cells.

4.1.3 Number of faces per cell. To identify the most representative shape of the cells in NiTECH foam, 3D image analysis was again performed. First, only the voxels of the skeleton that have two different cell labels in their neighbourhood are considered. A label is assigned to each face. Then, each in turn, faces

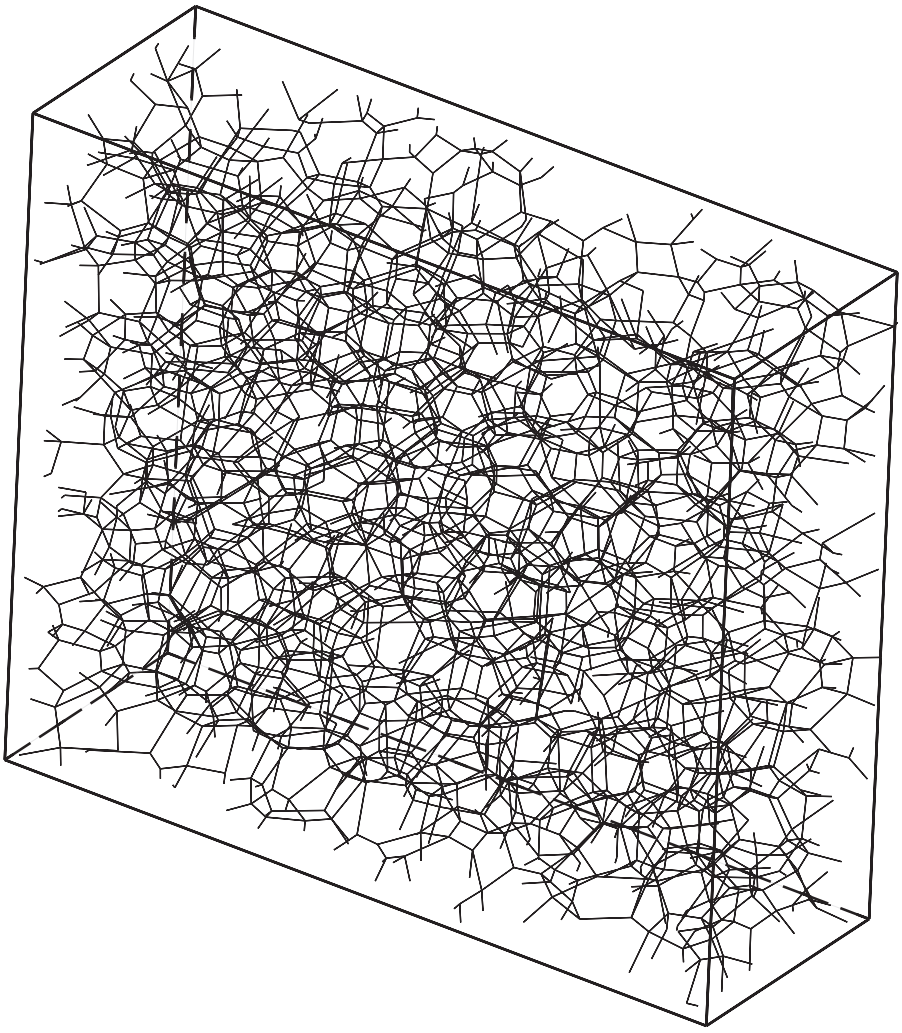

Figure 3. 3D graph of an open-cell foam derived from microtomographic analysis. It contains 143 complete cells.

are dilated isotropically. Nodes that are in the neighbourhood of the dilated face are recorded. The number of nodes is equal to the number of sides of the face. Moreover, the edges of the faces are removed and the core of the face is dilated. The cell labels met during this morphological operation are also recorded. As a result, for instance, the following information is obtained: the face labelled 1 has five sides and belongs to cells 1 and 4. Therefore, the number of faces per cell and the number of sides per face can be readily deduced.

Table 1 gives the distribution of the number of faces per cell. A sharp peak is observed for the value 12. One-third of the cells have 12 faces. However, the average number of faces per cell is found to be equal to

$$\langle f \rangle = 13.02 \tag{3}$$

One can also see that 80% of the values lie between 12 and 15 faces.

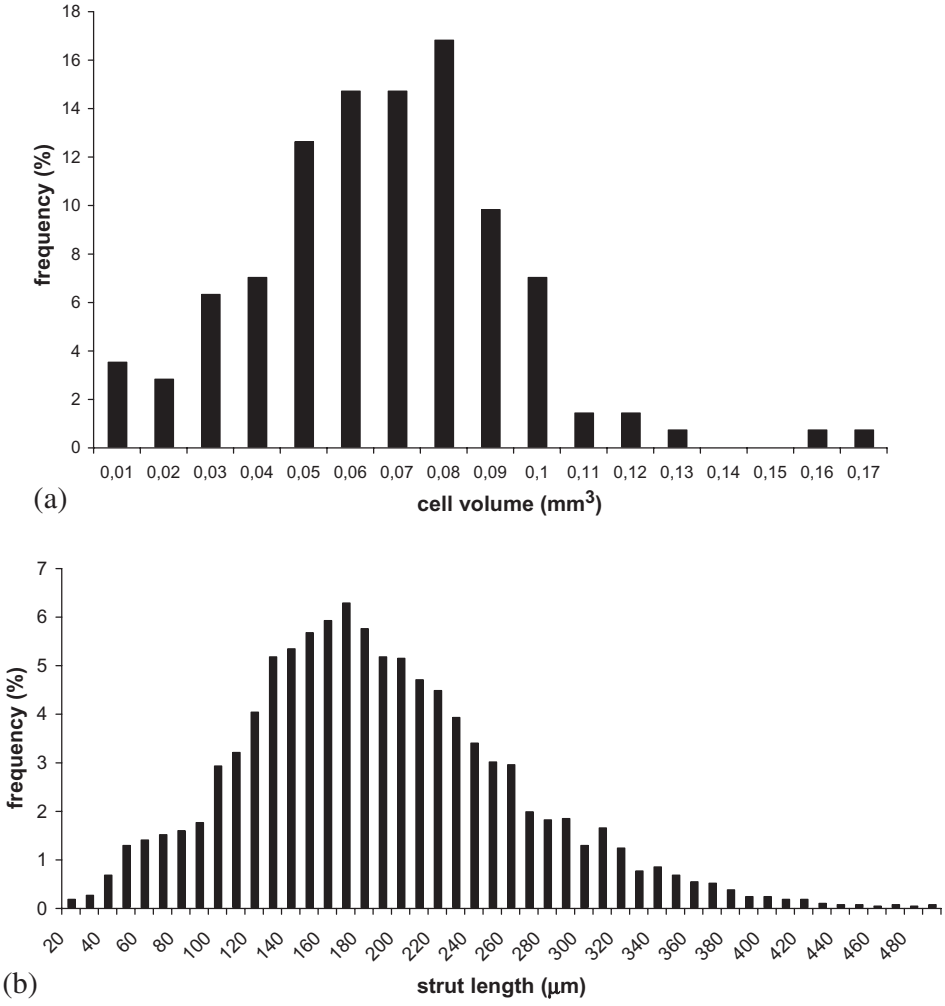

Figure 4. Cell volume distribution (a) and strut length distribution (b) in the initial state of nickel foams.

Table 1. Frequency (%) of the number of edges meeting at a node, number of edges per face, and number of faces per cell.

Property	1	2	3	4	5	6	7	8
Node coordination	13.9	4.5	8.8	71.5	0.7	0.4	0	0.2
Edges per face	0	0	0.9	17.6	56.8	21.8	2.8	0.1

	8	9	10	11	12	13	14	15	16	17	18
Faces per cell	1.7	0	3.3	6.7	33.3	18.3	20	8.3	5	1.7	1.7

Moreover, the shape of the most representative cell can be extracted from these results. The four most frequent cells encountered in the open-cell nickel foams are given in table 2. The most representative cell in NiTECH foams has 12 faces: two quadrilaterals, eight pentagons and two hexagons. The most frequent

Table 2. Shape of the most frequent cells in NiTECH open-cell nickel foams.

Shape	Frequency (%)	Total number of faces	Quadrilateral faces	Pentagonal faces	Hexagonal faces
1	15	12	2	8	2
2	11.5	12	0	12	0
3	8.3	14	2	8	4
4	6.6	13	3	6	4

cell is presented in figures 5a and b, where the 3D representation of the tomographic image is compared with the corresponding node–strut graph. Fifteen percent of the cells in the foam display this shape. The proportions of quadrilaterals and hexagons present in this cell are equal and represent 16.6%, whereas pentagons represent 66.6%.

4.1.4. Number of sides per face. Table 1 also gives the mono-modal distribution of the number of edges per face. Most of the faces of the foam are pentagonal. Pentagons represent 57% of the faces. There is about the same proportion of quadrilateral and hexagonal faces. There are 18% and 22% of faces with four and six sides in the foam, respectively. The average number of sides is equal to

$$\langle n \rangle = 5.07 \tag{4}$$

The results of sections 4.1.3 and 4.1.4 show that most of the NiTECH foam cells have 12 faces and that most of these faces are pentagonal. This shape is well represented in many foams (it is the second most frequent shape in NiTECH foam) even if pentagonal dodecahedra do not pack to fill space. As a result, the pentagonal dodecahedron is often chosen as the ideal cell to describe foams [25, 28].

4.1.5. Strut length distribution. The strut length is determined at the end of the 3D image analysis once the graph of the foam is obtained. Only the spatial positions of nodes and node connectivity are necessary to calculate the length of the struts. Figure 4b shows the distribution of strut length. It is mono-modal and spread. Fifty percent of the foam struts have a length ranging between 130 and 210 μm. Due to the long tail of the distribution, the mean strut length is 193 μm. However, the mono-modal strut length is around 170 μm, which is in good agreement with SEM observations [16]. The possible curvature of some struts is not considered in the computation, because it is seldom observed. Struts are regarded as straight lines connecting two nodes.

4.1.6. Equivalent ellipsoid size and orientation. The investigated cells are not isotropic. Their shape is controlled by material processing. Indeed, the foaming process of the polyurethane foam template is affected by the gravity effect, which favours cell elongation in the direction ND. During the nickel foam process, a tensile force is applied in the direction RD and can modify the cell shape. In order to quantify the corresponding anisotropy, cells are replaced by equivalent ellipsoids. The dimensions of the three axes of the ellipsoids as well as their orientations are determined according to the following procedure.

For each isolated cell in the 3D image, the 3D matrix of inertia is computed. The eigenvalues of this matrix are obtained and correspond to the three principal axes of

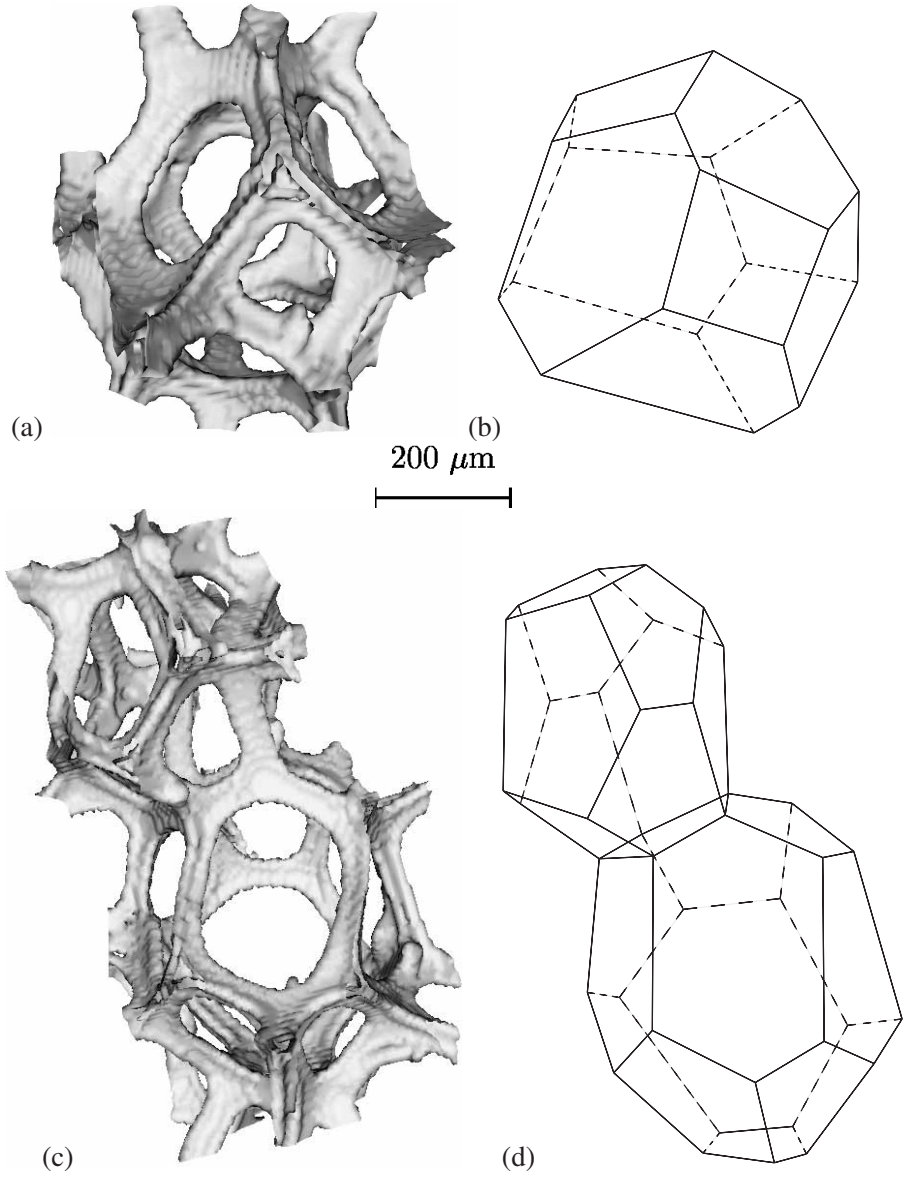

Figure 5. Most frequent cell in open-cell nickel foams: (a) 3D cell rendering, (b) associated skeleton. (c, d) Part of the Weaire–Phelan structure of open-cell nickel foams (3D rendering and associated skeleton, respectively).

the equivalent ellipsoid. For each cell, the three principal axes of the equivalent ellipsoid are denoted $a < b < c$ (see figure 6a).

Figure 7 shows the three mono-modal distributions of parameters a, b, and c for the initial state. As expected, the three dimensions of the equivalent ellipsoid are different. The distribution of the a parameter is the least scattered. The three distributions overlap. This overlap is more important between the distributions of the parameters b and c. The distribution of the c parameter is the most scattered.

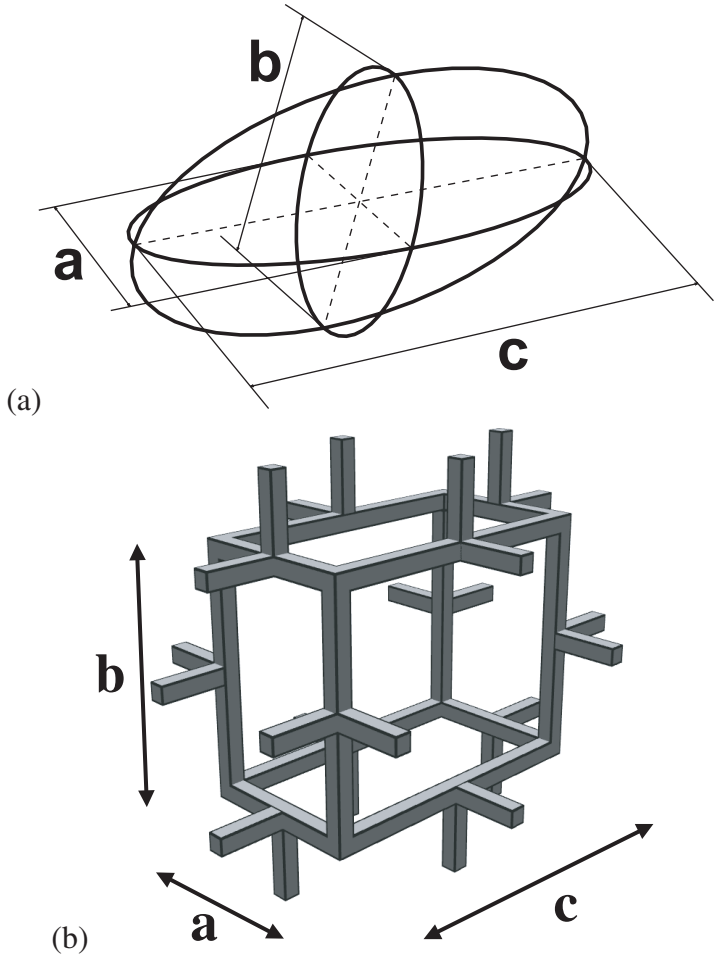

Figure 6. Idealized anisotropic unit cells: (a) equivalent ellipsoid, (b) idealized anisotropic beam network.

The average values of the three parameters a, b, and c are, respectively, 419 ± 12, 520 ± 14 and $632 \pm 17\,\mu$m. The volume of the ellipsoid with the three mean axes a, b and c is equal to $0.072\,\text{mm}^3$. This value is close to the mean cell volume found in section 4.1.1. The elongated shape of the cells is characterized by the ratios $c/a = 1.51$ and $c/b = 1.21$.

Finally, the eigenvectors of the moment of inertia matrix associated with the eigenvalues a, b, and c are computed and analysed. The stereographic projections of these vectors are presented in the plane (TD, RD) in figure 8. The orientation of the a axis of the equivalent ellipsoid of each cell is represented by a black spot in the plane (TD, RD) of the pole figure 8a. The orientations of the b and c axes for all equivalent ellipsoids are shown in figures 8b and c, respectively. Figure 8 clearly shows that the a axes of the ellipsoids (i.e. the shortest axes) are generally parallel to the transverse direction TD, b to the direction RD and c to the normal direction ND.

The fact that the ellipsoid directions associated with the largest axis (c parameter) are oriented in the normal direction ND is due to the foaming process of the polymer

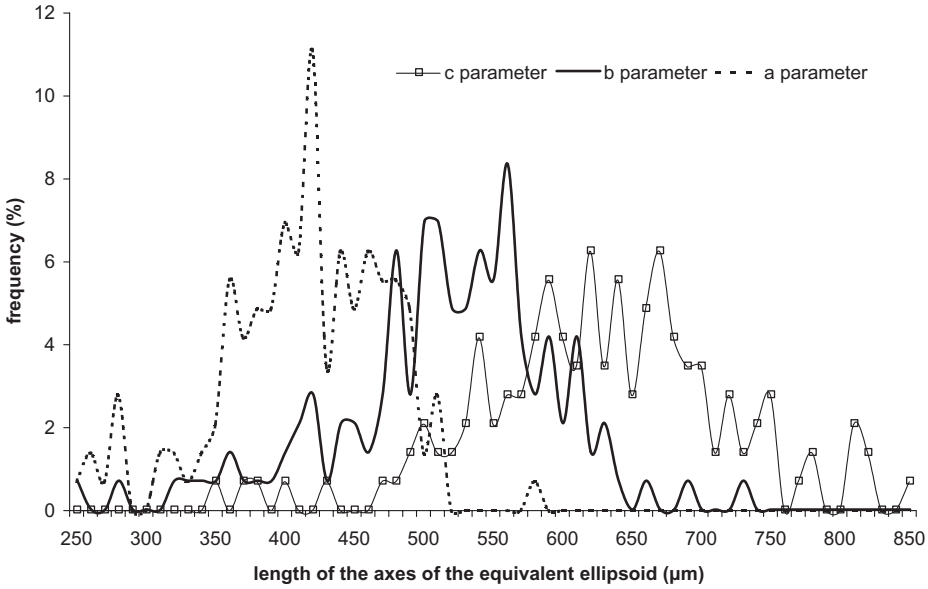

Figure 7. Length distribution of the axes of the equivalent ellipsoid for cells at the initial stage.

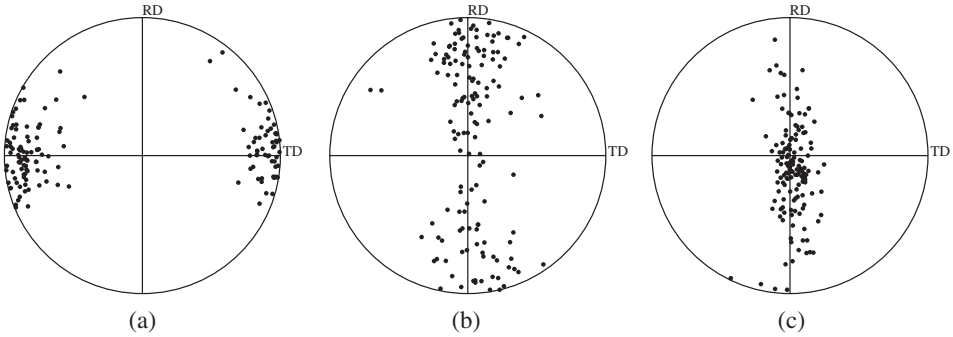

Figure 8. Orientation of the axes of the equivalent ellipsoids in the plane (TD, RD) at the initial stage: (a) *a* axes, (b) *b* axes, (c) *c* axes.

foam and the specific plane cut in the polymer foam block. During the manufacturing process, the force applied to the foam in the direction RD may explain why the eigenvector associated with the medium axis *b* is more or less aligned with the direction RD. The effect of the manufacturing process is also visible in the dispersion of the stereographic projections. During the manufacturing process, the cells may be tilted in the direction RD. This may explain why the orientation of the largest *c* axis is not always aligned with the normal direction, but is also scattered along the RD line (figure 8c).

4.2. *Tensile test in direction RD*

An *in situ* tensile test, in the direction RD, was performed. The overall experimental stress–strain curve is given in figure 9. After a linear elastic regime, open-cell nickel

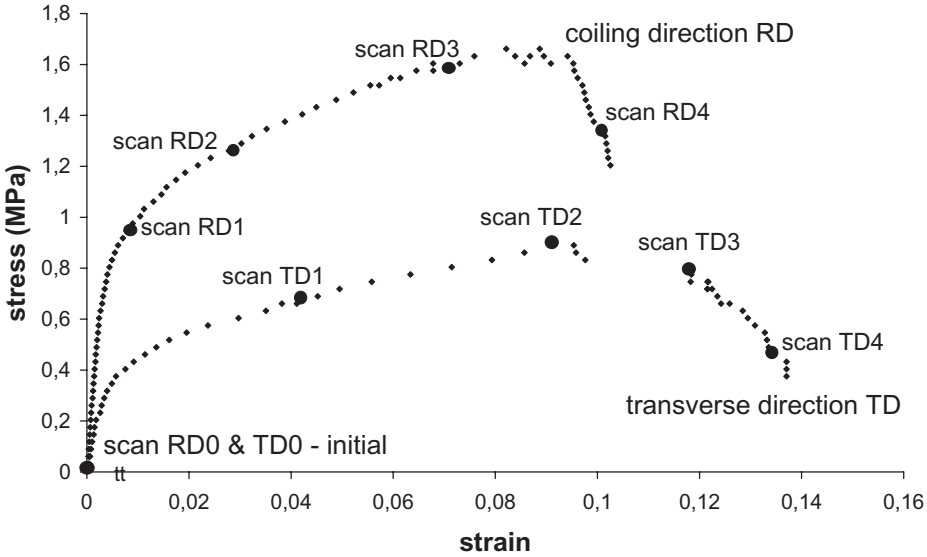

Figure 9. *In situ* tensile curves. Scan acquisitions during the tests are indicated by larger black dots and corresponding labels.

foams exhibit a nonlinear elastoplastic regime followed by a regime with almost linear hardening [16]. A tomographic scan was performed in each part of the curve to better understand the deformation mechanisms. The positions of these scans are indicated by black dots in figure 9. The scan RD0 represents the initial state. Scan RD1 is placed at the very beginning of the plastic regime, scan RD2 in the plastic regime and scan RD3 at the onset of fracture. Scan RD4 was taken when a large crack had propagated.

The 3D rendering of the microstructure of the material at two deformation stages is presented in figure 10. The tensile direction of the test is vertical. The foam elongates in the vertical direction, whereas contraction is observed in the horizontal direction. A crack initiates at the top of the specimen (scan RD3). In tension, before cracking, the cells do not undergo large deformations. The observation of the deformation of individual cells indicates that no significant pure bending is visible. Only a relative displacement between nodes and some alignment of struts in the tensile direction can actually be seen. To highlight the small rotation of the struts, the graph of one cell and its evolution during straining are shown in figure 11a. The dotted and solid lines correspond to the initial and deformed structures of the cell, respectively. The alignment of struts with the vertical direction and cell elongation can be clearly seen.

The crack clearly visible on scan RD4 was already initiated in scan RD3. The net section of the sample decreases, whereas the overall stress still increases (figure 9). This may be explained by the competition between strut alignment and work hardening, on the one hand, and failure of struts, on the other.

4.3. *Tensile test in direction TD*

The same analysis was carried out for a tensile test along TD. The *in situ* tensile curve, during loading in the transverse direction TD, is given in figure 9.

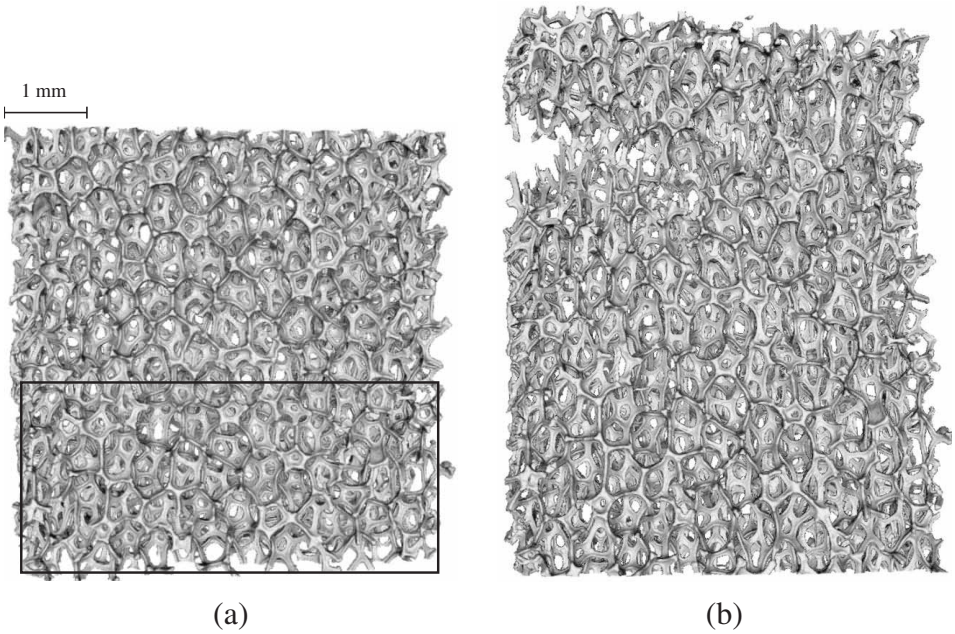

Figure 10. 3D renderings of the tensile test along RD: (a) scan RD0, (b) scan RD4. The tensile direction is vertical.

The mechanical behaviour of open-cell nickel foams exhibits a strong anisotropy effect. Indeed, Young's and the plastic moduli depend on the tensile direction. Failure stress during tension in direction RD (1.6 MPa) is almost twice the value found in direction TD (0.9 MPa). Strain at failure is around 7% in direction RD and 9% in direction TD.

Five scans were recorded during the test (see figure 9): one in the initial state without deformation, one in the middle of the plastic regime, one just before and one just after crack initiation, and the last one before the end of the test. Overall 3D reconstructions of this tested foam are shown in Dillard *et al.* [13]. A zoom of the middle part of the sample is shown at different strain levels in figure 12. It can be seen that the struts rotate around the nodes and line up slightly along the loading direction. This relative rotation induces bending at the nodes and leads mainly to the fracture of junctions. Struts where displacement is noticeable are marked with black arrows. Fractured junctions are marked with dotted arrows.

The question of the representativeness of the considered samples for tension along RD and TD can be raised due to the small thickness and width of the samples: 12 to 13 cells within the width and three to four cells within the thickness. We have checked, in fact, that the tensile curves of figure 9 are close to the curves obtained with larger foam strips in tension. The latter curves can be found in Badiche *et al.* [16]. The comparison shows that fracture takes place earlier in the small sample for tension along TD, but later for RD. The difference, however, lies within the scatter of the ductility of the considered nickel foam. Accordingly, the tensile curves of the small samples can be regarded as representative of the overall behaviour of the foam. This suggests that the usual rule of thumb for foams stating that representative volumes should contain at least 10×10 cells within the section is not a necessary

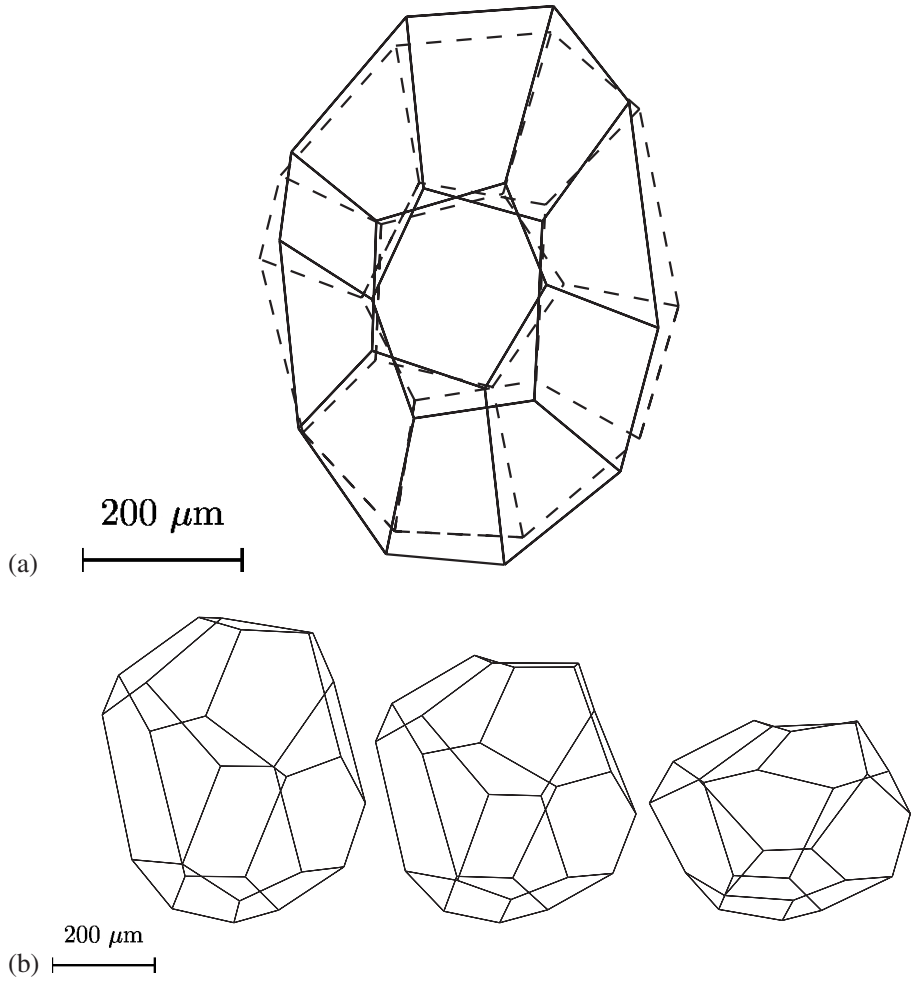

Figure 11. Individual cell deformation: (a) in tension along RD, superimposition of scans RD0 (dotted line) and RD4 (solid line); (b) different states of one cell in compression (scans COMP0, COMP1 and COMP2). In both cases the loading direction is vertical.

condition. If a high enough number of cells is present within the sample width, a smaller number of cells within the thickness can be sufficient for the sample to be representative.

4.4. *Compression test*

The *in situ* compression curve is presented in figure 13. Black dots indicate the position of the scans. Compression of open-cell nickel foams exhibits three main stages: an initial linear elastic regime at low stresses, followed by a stress peak and a decrease of the stress, and, finally, a densification regime in which the stress rises steeply. The slope of the beginning of the curve is different from the linear elastic slope, due to the irregular and not exactly parallel surfaces of the foam sample.

The 3D renderings of four scans are shown in figure 14. The 3D morphology of the initial state is given by the scan COMP0. The scan COMP1 coincides with the

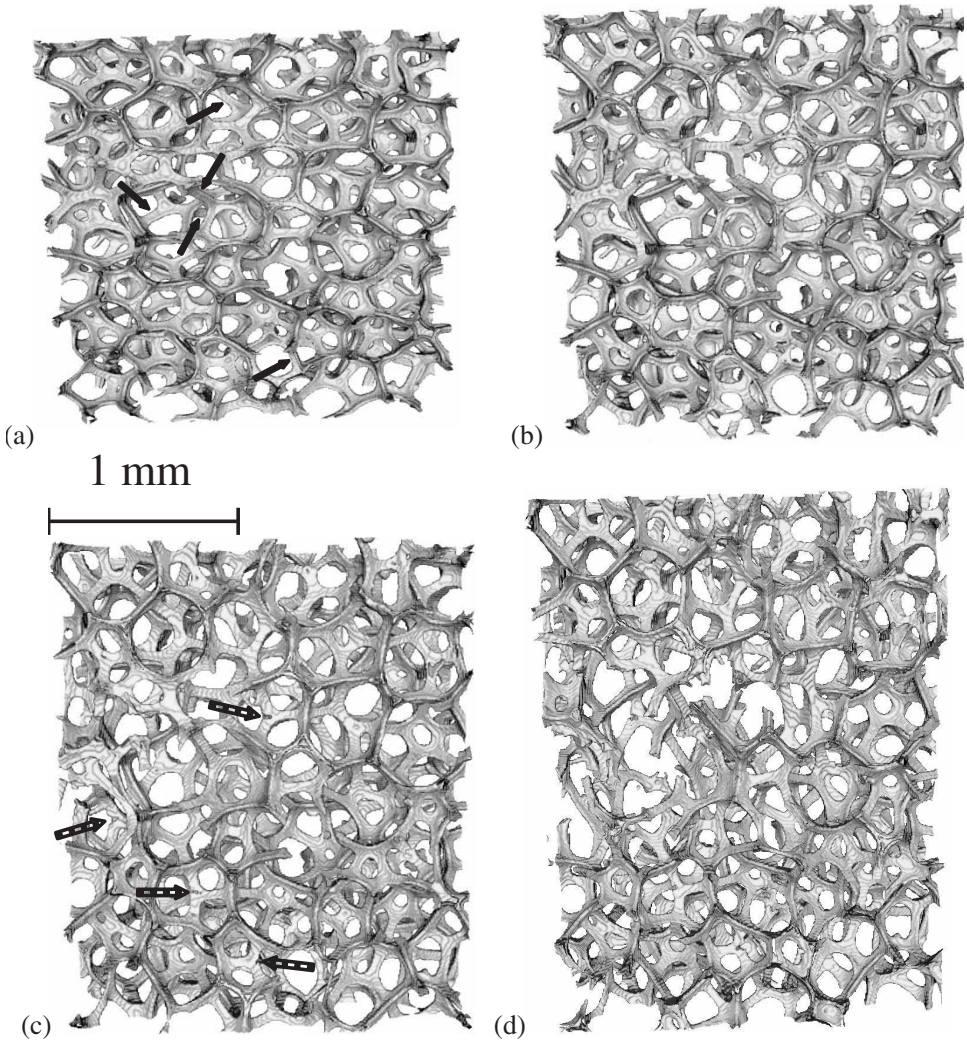

Figure 12. 3D rendering of the TD scans: (a) scan TD0, (b) scan TD2, (c) scan TD3, (d) scan TD4. The black arrows denote struts that undergo significant displacements. The dotted arrows indicate cracks.

stress peak. Scan COMP2 is close to the stress minimum after the peak of the curve, whereas scans COMP3 and COMP4 were taken at different levels of densification. The direction of compression is vertical. At low stresses, small amounts of bending are observed until the stress peak. Buckled struts, marked by arrows in scan COMP1, are longer, still aligned with the compression direction, and relatively localized in the same horizontal plane. In scan COMP1 (peak stress), buckled struts are clearly visible. That is why the stress decreases. Deformation of the buckled struts is localized in a small part of the struts. This is different from the severe bending observed by Elliott *et al.* [8] in polymer foams. In scan COMP2, cells have almost completely collapsed. The densification regime begins when a band of strain localization develops. The cells located in the foam core are totally collapsed (scan COMP3), whereas cells located at the top and the bottom of the sample are still

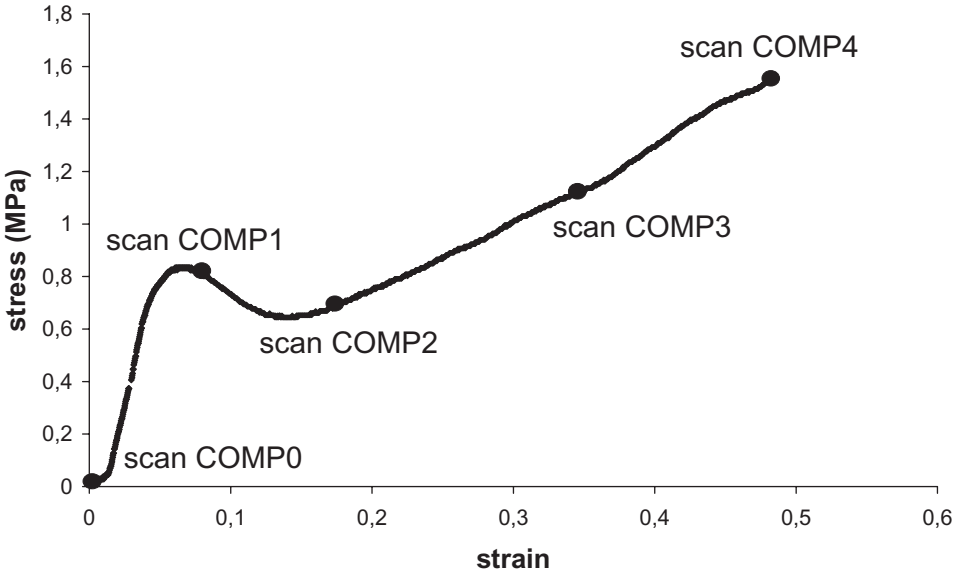

Figure 13. *In situ* compression curve.

undeformed until a high level of compression (scan COMP4). To analyse the deformation better, an individual cell of the foam core has been isolated from the graph representation at different strain levels in figure 11b. Note that the node–strut graph representation does not take strut bending or buckling into account.

The formation of a strain localization band in compression can be further evidenced by looking at the TDR evolution (see equation (2) for the definition of this parameter). For that purpose the surface fraction of nickel is computed for each slice of the 3D image parallel to the free surface. This quantity can be used to compute a TDR for each section, defined as the ratio of the density of the current slice divided by the density close to the free surface. This is an extension of definition (2). The evolution of the nickel surface density is plotted for the five scans in figure 15. At the initial state, the classical curve of the nickel quantity through the sample thickness is retrieved. The nickel quantity is maximal at the surface of the foam. It then decreases and remains almost constant in the mid-section of the foam. The thickness of this region with low nickel content is about 600 μm, which represents more than one-third of the sample thickness. Strain localization clearly takes place in this part of the sample where TDR is initially minimum. A bump appears in the mid-section of the foam in scan COMP2. This means that the cells located in the mid-section of the foam are crushed. The nickel quantity is thus increased in this region. The nickel quantity present at the surface of the foam remains unchanged during the compression test, which is in good agreement with the qualitative observations.

5. Discussion

The discussion concentrates on four specific issues. The first subsection compares the morphology of the cells found in this work with other observations from the

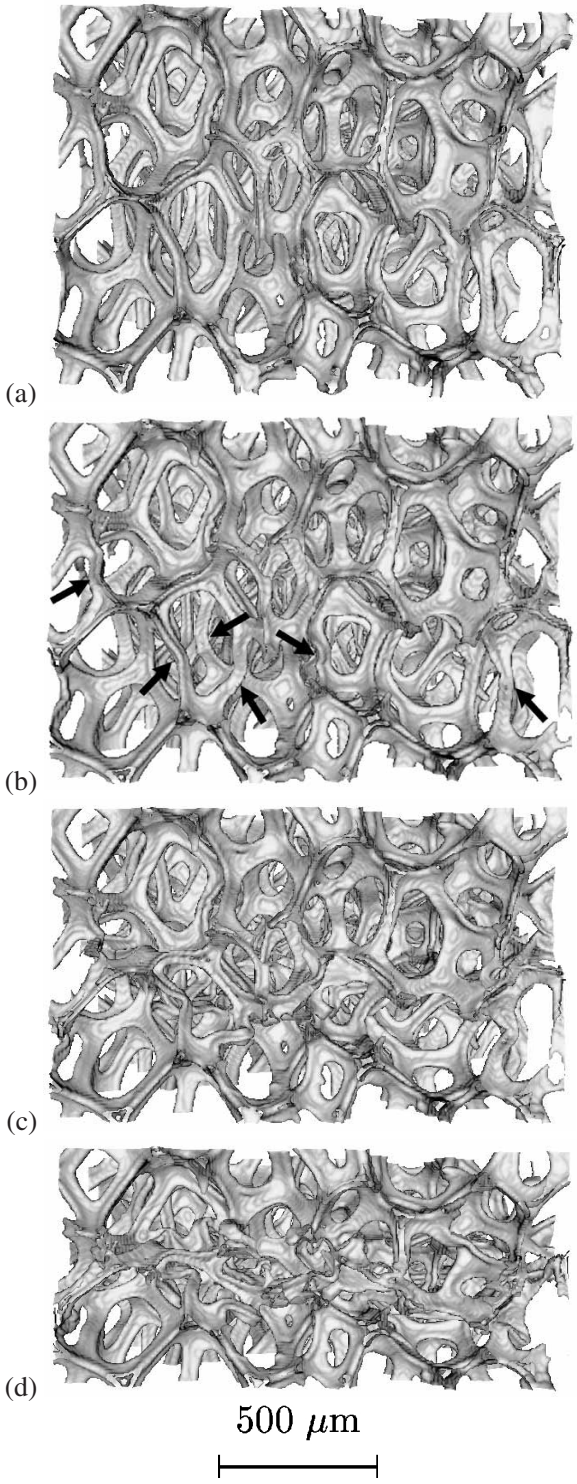

Figure 14. 3D rendering of the compression scans: (a) scan COMP0, (b) scan COMP1, (c) scan COMP2, (d) scan COMP3. The vertical direction is parallel to ND.

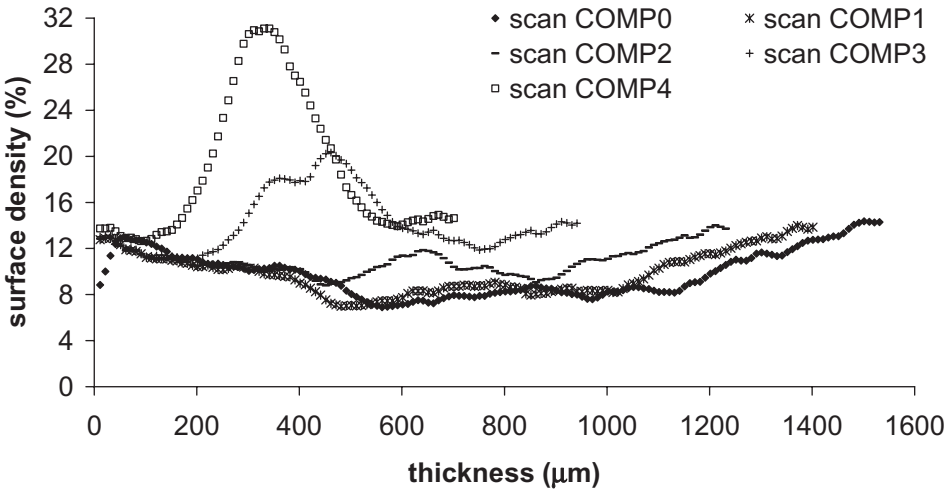

Figure 15. Evolution of the nickel surface density for all sections normal to direction ND during a compression test.

literature. The second subsection attempts to relate the observed anisotropy of the cells' shape to the anisotropy of the mechanical behaviour of the material. The evolution of the cell orientation during straining is analysed in detail in section 5.3. The last issue is a description of the damage and cracking mechanisms.

5.1. *Typical cell shape in nickel foams: comparison with soap bubbles*

According to Thomson [29], the cell that minimizes the surface energy and can fill space in an ideal monodisperse foam is a tetrakaidecahedron. Kelvin's tetrakaidecahedron is composed of 14 faces: eight hexagons and six quadrilaterals. No ideal Kelvin cell was found in the NiTECH foam. This result was already noted by Matzke [30]. Matzke determined the structure of 1000 bubbles of a soap foam by looking at photographs (400 bubbles belonging to the first three layers and 600 other bubbles located inside the foam). One possible reason for the absence of Kelvin's tetrakaidecahedron may be found in Weaire and Phelan [31]. The Kelvin cell assembly is eventually not the lowest surface energy structure. Indeed, Weaire and Phelan have found an assembly of cells with a surface 0.3% smaller than Kelvin's, but this assembly is not made of identical cells. It is composed of eight cells: two pentagonal dodecahedra and six tetrakaidecahedra. The Weaire–Phelan tetrakaidecahedron is different from Kelvin's. It has 12 pentagons and two hexagons. The Weaire–Phelan tetrakaidecahedron and pentagonal dodecahedron have been observed close together in NiTECH foams. Figures 5c and d show the 3D rendering of the assembly of these two cells and the corresponding network. However, the whole structure with the eight cells is not present in the foam and only a few Weaire–Phelan tetrakaidecahedra are observed. NiTECH foams contain a larger proportion of pentagonal dodecahedra.

Table 3 gives the average number of sides per face and the average number of faces per cell resulting from different observations in the literature [30, 32] or theories based on minimizing the surface area of foams. The Matzke and Monnereau values given in the table are for bulk bubbles. For surface bubbles, that is the first three

Table 3. Mean number of faces per cell $\langle f \rangle$ and number of edges per cell $\langle n \rangle$ for five types of foams.

	Kelvin [29]	Weaire–Phelan [31]	Matzke [30]	Monnereau [32]	This work
$\langle f \rangle$	14	13.39	13.7	14.3	13.02
$\langle n \rangle$	5.14	5.10	5.12	5.16	5.07

layers, the average number of faces per cell $\langle f \rangle$ is about 11. One can see that the average number of faces per cell is higher in the study of Monnereau *et al.* [32], but only nine bubbles were reconstructed. Table 3 shows that the average number of sides per face varies less than the average number of faces per cell, and that our data are in good agreement with those found in the literature. They are lower than those calculated for the Weaire–Phelan structure and the minimum values found in Aste *et al.* [33]. According to Aste *et al.* [33], a value of $\langle f \rangle = 13.3$ corresponds to the minimal free energy in tetrahedrally close-packed (TCP) structures [34].

Another point of Matzke's study can be compared with the results obtained for NiTECH foams. Matzke found that 99% of the cells have between 12 and 15 faces. We find only 80% in our study. He also found that the proportion of pentagons is around 60% and that hexagons are more numerous than quadrilaterals. These observations are in good agreement with our results. However, the comparison is difficult to make because the relative density of Matzke's foam is not known. One can also note that Euler's equation [35], i.e. the relationship between the number of sides per face and the number of faces per cell, is well satisfied in our study:

$$\langle n \rangle = 6 - \frac{12}{\langle f \rangle} = 6 - \frac{12}{13.02} = 5.078 \tag{5}$$

As a conclusion of this section, one can state that the results for the topology of NiTECH foams are roughly similar to those found for soap bubbles. Phenomena such as drainage and gravity, responsible for the shape of the cells, are similar for soap bubbles and for polyurethane foams.

5.2. *Geometrical versus mechanical anisotropy*

The anisotropy of the elastic properties of foams has been related to a geometric parameter by Gibson and Ashby [14] using a simple beam model. These authors introduced an idealized quadratic unit cell as in figure 6b with $a = c$. They estimated the overall properties as a function of the geometry aspect ratio $R = b/a$. Badiche *et al.* [16] studied the anisotropy of the electrical and mechanical properties of open-cell nickel foams very similar to the present ones. They deduced a geometry aspect ratio $R = 1.5$ from the Gibson and Ashby model and experimental results. They expect the cell to be 1.5 longer along direction RD than along direction TD. According to section 4.1.6, the 'average' aspect ratio is, in our case,

$$R = \frac{b}{a} = \frac{520}{419} = 1.24 \tag{6}$$

This difference is probably due to the choice of a tetragonal unit cell in Badiche *et al.* [16] ($a = c$), which is not really representative of the equivalent ellipsoid parameters reported in the present work. To show this, the same analysis as in Gibson and

Ashby [14] is performed to estimate the ratio of longitudinal and transverse Young's moduli, but using the orthotropic unit cell of figure 6b.

The ratio of Young's moduli is expressed in terms of two geometrical parameters, R and Q, defined as

$$R = \frac{b}{a}, \qquad Q = \frac{c}{a} \tag{7}$$

Let us label a, b, c the edges of the cell with lengths a, b, c, respectively, in figure 6b. During loading in direction b, the edges a and c are bent due to forces F_a and F_c, respectively. The total force $F = F_a + F_c$ is assumed to be related to the overall stress component σ_{bb} acting on the foam:

$$F = F_a + F_c \propto \sigma_{bb} ac \tag{8}$$

Shearing and tension of the beams are neglected. The deflections of the edges are therefore proportional to

$$\delta_a \propto \frac{F_a a^3}{E_{\mathrm{Ni}} I}, \qquad \delta_c \propto \frac{F_c c^3}{E_{\mathrm{Ni}} I} \tag{9}$$

where E_{Ni} is Young's modulus of bulk nickel and I is the moment of inertia of the strut. We assume that the displacement $\delta_a = \delta_c$ is prescribed and related to the overall strain ε_{bb} in the direction of the b axis of the foam:

$$\delta_a = \delta_c \propto \varepsilon_{bb} b \tag{10}$$

Young's modulus E_b in tension along direction b is obtained as

$$E_b = \frac{\sigma_{bb}}{\varepsilon_{bb}} \propto E_{\mathrm{Ni}} I \frac{b}{ac}\left(\frac{1}{a^3} + \frac{1}{c^3}\right) \tag{11}$$

Young's modulus E_a in direction a is obtained by permutation of a and b. As a result, assuming that the proportionality factor in equation (11) is the same for directions b and a, the ratio of Young's moduli is equal to

$$\frac{E_b}{E_a} = \frac{b^2}{a^2}\left(\frac{(1/a^3) + (1/c^3)}{(1/b^3) + (1/c^3)}\right) = R^2 \frac{1 + (1/Q^3)}{(1/R^3) + (1/Q^3)} \tag{12}$$

If $Q = 1$, the result $E_b/E_a = 2R^2/(1 + 1/R^3)$ obtained in Gibson and Ashby [14] is retrieved.

The results obtained from 3D image analysis can now be used to estimate the ratio defined by equation (12). It is shown that the directions a, b, c of the cells are mainly parallel to the directions TD, RD, and ND, respectively. Taking the average values of a, b and c found in section 4.1.6, we predict a ratio $E_b/E_a = E_{\mathrm{RD}}/E_{\mathrm{TD}} = 2.44$.

Experimental results are available for Young's moduli from tensile tests in directions RD and TD [36]:

$$E_b = E_{\mathrm{RD}} = 537 \pm 29\,\mathrm{MPa}, \quad E_a = E_{\mathrm{TD}} = 182 \pm 8\,\mathrm{MPa} \tag{13}$$

The ratio is therefore $E_b/E_a = 2.95 \pm 0.3$. This is in reasonable agreement with the predicted value.

5.3. *Evolution of cell dimensions and orientation during tension*

In this section, the evolution of the dimensions and orientations of the cells during loading is discussed. The analysed volumes are indicated by black boxes in the 3D rendering images (see scan RD0 of figure 10). The dimensions of these boxes are 2.3 mm height, 4.9 mm width and 1.68 mm thickness for tensile test in direction RD and 2 mm height, 3.9 mm width and 1.68 mm thickness for tensile test in the transverse direction. They contain, respectively, 123 and 76 cells. Incomplete border cells are again excluded.

As explained in section 4.1.6, the three axes of the equivalent ellipsoid (a, b, c) are determined for each cell at different strain levels. The mean values of these three parameters are given in table 4 at each deformation stage. Scans RD4, TD3 and TD4 are not included because crack initiation makes the results difficult to interpret.

When loading is applied in direction RD, the a parameter decreases, the b parameter increases slightly and the c parameter remains almost the same. Fluctuations of the three parameters are small. Figure 16 presents the orientation of the axes of a, b and c in the plane (TD, RD). At the initial state, the orientation distribution is similar to that found in section 4.1.6 (figure 8). In the initial state, the a axes are oriented along the transverse direction, the b axes are more or less parallel to the direction RD and the c axes are oriented normal to the foam sheet. Therefore, during the tensile test in direction RD, the parameter b should increase, whereas the two others should decrease. Table 4 shows that the a parameter is decreasing, but the expected trend is not clear for parameter c. This is due to the fact that cells are not simply stretched, but undergo significant rotations. This is especially true for the c vectors, as shown in figure 16. The c axes align more and more with direction RD. Only the a axes seem to keep their initial orientation. During loading, their distribution tightens close to the pole TD. One can therefore consider that the evolution of the a parameter represents deformation of the material in the transverse direction when tension is along direction RD. The maximal deformation of the mean a parameter, just before cracking between scans RD0 and RD3, using the data of table 4, is 4%.

The same orientation of the initial state is obtained for scan TD0 (see figure 17). When loading is applied in the transverse direction, the a parameter should increase, whereas the parameters b and c should decrease. This is actually what table 4 shows. The cells become more isotropic and the orientation of the axes is more uniformly distributed in space. Scan TD2 of figure 17 illustrates this phenomenon. The distribution of the orientations of the three parameters becomes rather random.

5.4. *Damage and cracking*

As explained in section 4.2 and illustrated in figure 12, the rotation of struts induces damage during tensile tests. Fracture takes place at the nodes of the foam. This failure at junctions can be clearly seen in figure 18 at a resolution of 2 μm. This may be due to high stress concentrations at nodes. Damage is distributed in a small area. The characteristic length of the crack area is about five cells (see figure 12).

In open-cell nickel foams, the first crack always initiates at a lateral boundary of the sample. This phenomenon may be due to the larger relative displacement of

Table 4. Evolution of the mean values of the three axes of the equivalent ellipsoid for all analysed cells.

Load	Loading direction	Scan number	a (μm)	b (μm)	c (μm)	$R = b/a$
Tension	RD	0	404 ± 12	511 ± 14	624 ± 17	1.28 ± 0.07
		1	404 ± 12	513 ± 14	621 ± 16	1.28 ± 0.07
		2	401 ± 12	525 ± 14	627 ± 16	1.32 ± 0.07
		3	388 ± 13	521 ± 17	627 ± 20	1.36 ± 0.09
	TD	0	406 ± 15	521 ± 20	611 ± 21	1.29 ± 0.1
		1	428 ± 16	521 ± 19	607 ± 20	1.22 ± 0.09
		2	447 ± 18	514 ± 18	594 ± 19	1.16 ± 0.09
Compression	ND	0	405 ± 20	509 ± 26	620 ± 31	1.26 ± 0.04
		1	408 ± 21	500 ± 24	604 ± 29	1.23 ± 0.04
		2	379 ± 22	465 ± 22	595 ± 28	1.24 ± 0.05

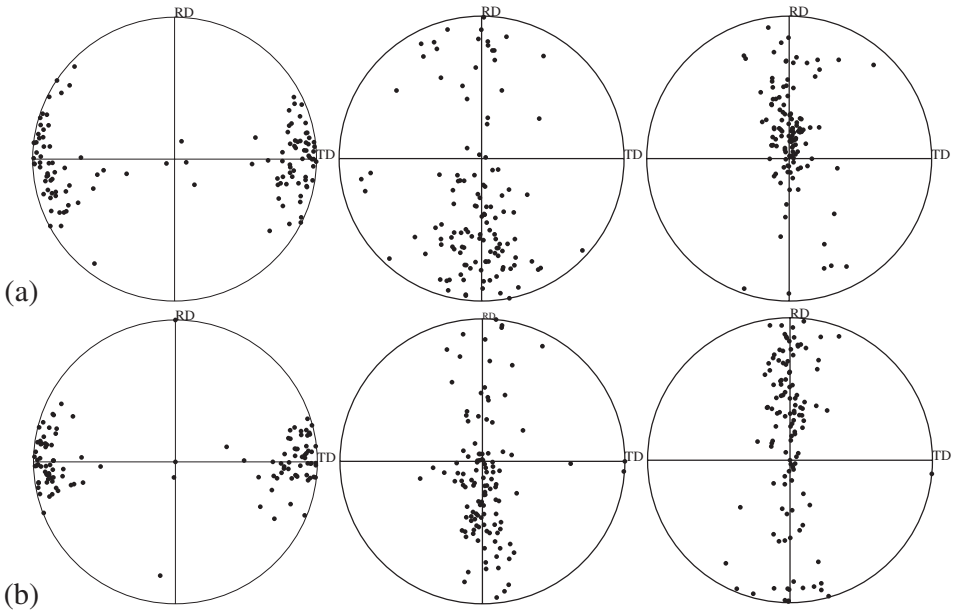

Figure 16. Evolution of the orientation of the axes of the equivalent ellipsoids in the plane (TD, RD) during a tensile test in the direction RD—*a* axis (left), *b* axis (middle), *c* axis (right): (a) scan RD0, (b) scan RD3.

the nodes of the struts located at the boundary. Indeed, these struts have one tip that can move readily because it is not constrained by a neighbouring cell. Alignment of struts, which leads to crack initiation, is much more significant at the lateral boundaries of the foam. Figure 19 shows this free edge effect. The initial and deformed stages are represented for the same area located at the boundaries of the foam. One can observe significant displacement of the unconstrained lateral struts.

When a crack initiates, a strut is broken and the load is redistributed over the next cells. The crack propagates cell by cell. However, some struts still bridge

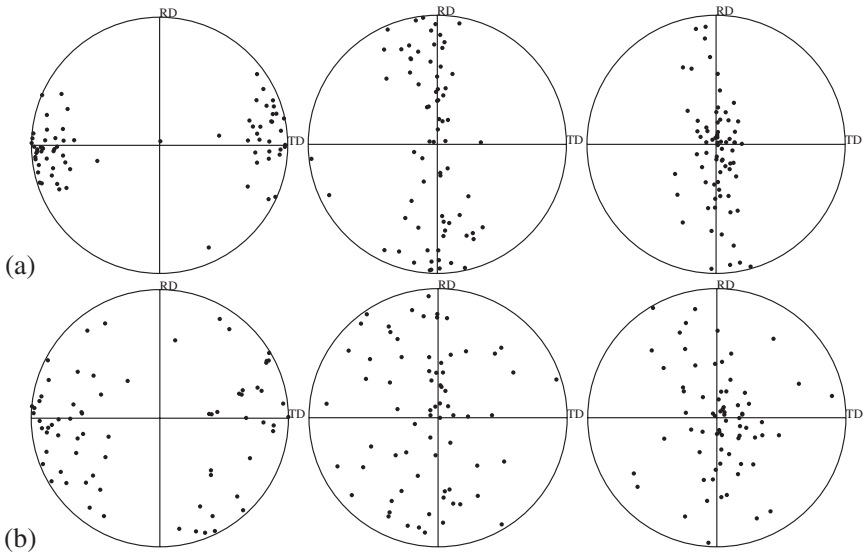

Figure 17. Evolution of the orientation of the axes of the equivalent ellipsoids in the plane (TD, RD) during a tensile test in the transverse direction—*a* axis (left), *b* axis (middle), *c* axis (right): (a) scan TD0, (b) scan TD2.

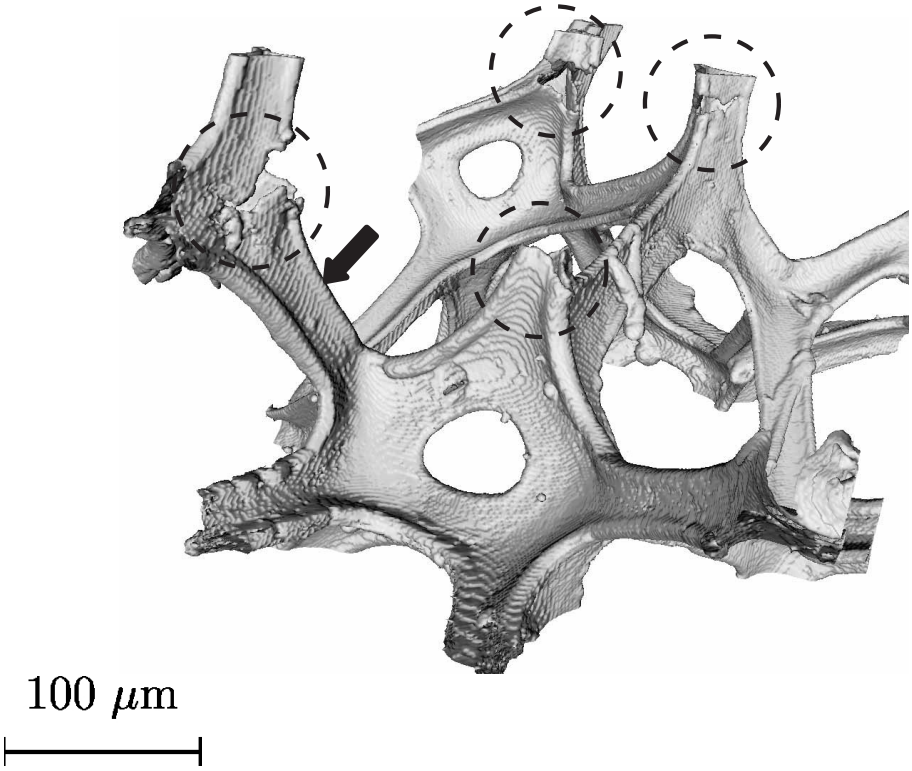

Figure 18. 3D rendering of a few cells at a resolution of 2 μm showing the initiation of cracks at junctions.

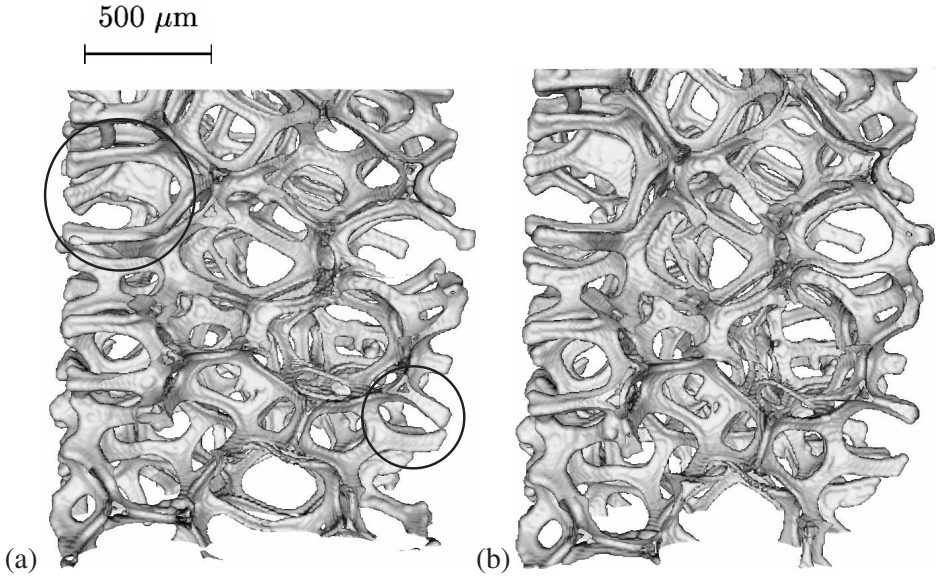

Figure 19. Free edge effect—lateral boundaries: (a) scan TD0, (b) scan TD2.

the crack, as shown in the dotted box of figure 20. This may again be explained by the competition between strut alignment and strut hardening.

6. Conclusions

In this work, X-ray microtomography, at a sufficiently fine resolution, is shown to be a technique well suited to study the morphology, and also the mechanical behaviour and fracture mechanisms, of open-cell nickel foams. The following information was obtained concerning the cell morphology of the investigated NiTECH open-cell foam:

- the average cell volume and strut length are, respectively, 0.071 mm^3 and 193 μm; note that the strut length can only be assessed by 3D measurements;
- the average number of faces per cell is 13; one-third of the cells are dodecahedra; the average number of sides per face is five; 57% of the faces are pentagonal;
- the most frequent cell in the foam is a dodecahedron with two quadrilaterals, two hexagons and eight pentagons.

The dimensions and orientation of the equivalent ellipsoid for each cell have been determined. The corresponding mean values of the three orthogonal axes in the initial state are 419 μm in the transverse direction, 520 μm in direction RD and 632 μm in the normal direction. This strong geometrical anisotropy determined by X-ray microtomography is due mainly to the initial polymer foam morphology and, to a smaller extent, to the nickel foam processing. It has been related to the observed mechanical anisotropy using a simple beam model. More elaborate mechanical models are needed, however, to account for the aspects

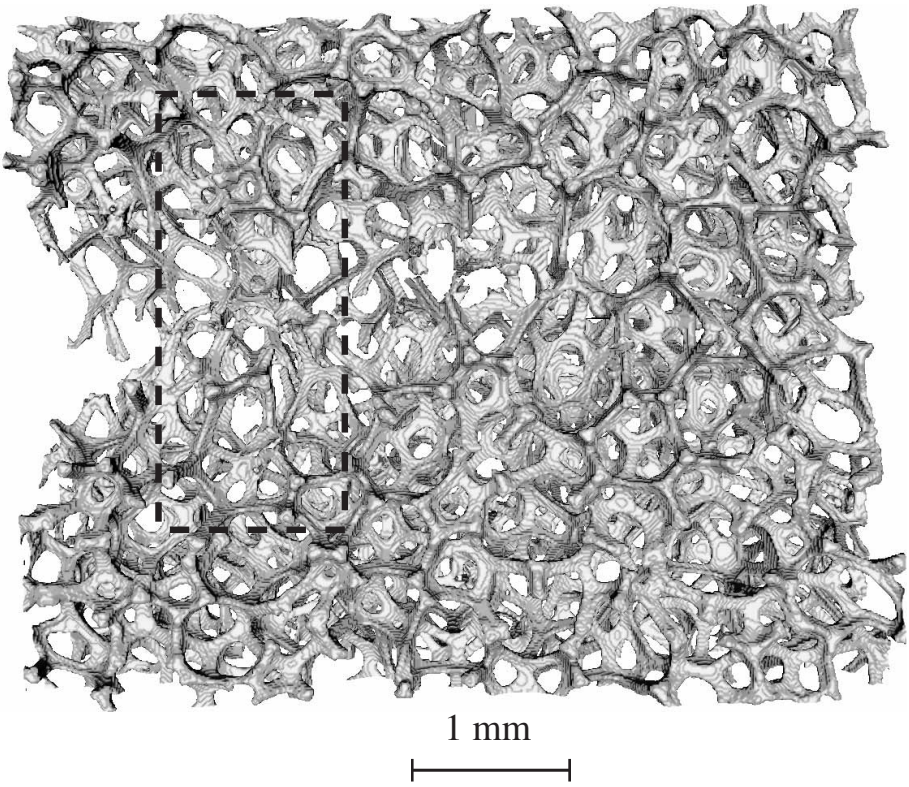

Figure 20. Zoom view at the fractured area (scan RD4). The crack comes from the left and the crack tip is in the middle of the image. The marked region contains unbroken struts still bridging the crack.

of plastic deformation evidenced in the present work such as cell shape and orientation evolution induced by plasticity.

The main deformation mechanisms are the following: bending, stretching and alignment of struts in tension; buckling of the struts more or less parallel with the loading direction in compression. Strong strain localization is observed in compression, whereas, in tension, deformation of nickel foams remains quite homogeneous before the initiation of final cracks. Pole figures of the axes of the equivalent ellipsoids of many cells were provided. They show that a tensile test in the direction RD reinforces some privileged orientations of the cells. In contrast, a tensile test in the direction TD leads to a significantly more isotropic distribution of cells.

Damage and fracture mechanisms were also observed. The cracks initiate at the lateral boundaries of the specimen (free edge effect). Failure starts mainly at nodes. The damaged area around the crack tip has a radius of about five cells. Crack propagation proceeds cell by cell, but some struts still bridge the crack.

The 3D graph of the foam samples (see figure 3) can now be used to construct finite element meshes of the foams as beam networks [6, 8]. This mechanical description will be used in further studies to predict the response of the foam in the elastic, plastic and failure regimes. The information obtained by microtomography can also be used for more simple micromechanical models in the nonlinear regime as proposed in Dillard [36].

Acknowledgements

The authors thank C. Lantuéjoul (Centre de Morphologie Mathématique, Ecole des Mines de Paris) for stimulating discussions concerning image analysis. They also acknowledge the European Synchrotron Radiation Facility for provision of synchrotron radiation facilities and especially the team of beam line ID19. The authors acknowledge the financial support of the French Ministry for Industry under contract MONICKE.

References

[1] H. Bart-Smith, A.-F. Bastawros, D.R. Mumm, *et al.*, Acta mater. **10** 3583 (1998).
[2] A.-H. Benouali and L. Froyen, in *Cellular Metals and Metal Foaming Technology*, edited by J. Banhart, M.F. Ashby and N.A. Fleck (MIT Publishing, Berlin, 2001), pp. 269–272.
[3] D. Leitlmeier and H. Flankl, in *Cellular Metals and Metal Foaming Technology*, edited by J. Banhart, M.F. Ashby and N.A. Fleck (MIT Publishing, Berlin, 2001), pp. 277–281.
[4] E. Maire, L. Babout, J.-Y. Buffière, *et al.*, Mater. Sci. Engn A **319–321** 216 (2001).
[5] E. Maire, A. Fazékas, L. Salvo, *et al.*, Composites Sci. Technol. **63** 2431 (2003).
[6] T.G. Nieh, J.H. Kinney, J. Wadsworth, *et al.*, Scripta mater. **38** 1487 (1998).
[7] T.G. Nieh, K. Higashi and J. Wadsworth, Mater. Sci. Engng A **283** 105 (2000).
[8] J.A. Elliott, A.H. Windle, J.R. Hobdell, *et al.*, J. Mater. Sci. **37** 1 (2002).
[9] A. Elmoutaouakkail, L. Salvo, E. Maire, *et al.*, in *Cellular Metals and Metal Foaming Technology*, edited by J. Banhart, M.F. Ashby and N.A. Fleck (MIT Publishing, Berlin, 2001), pp. 245–250.
[10] L. Helfen, T. Baumbach, H. Stanzick, *et al.*, in *Cellular Metals and Metal Foaming Technology*, edited by J. Banhart, M.F. Ashby and N.A. Fleck (MIT Publishing, Berlin, 2001), pp. 239–244.
[11] E. Jasiunienë, J. Goebbels, B. Illerhaus, *et al.*, in *Cellular Metals and Metal Foaming Technology*, edited by J. Banhart, M.F. Ashby and N.A. Fleck (MIT Publishing, Berlin, 2001), pp. 251–254.
[12] O.B. Olurin, M. Arnold, C. Körner, *et al.*, Mater. Sci. Engng A **328** 334 (2002).
[13] T. Dillard, F. N'Guyen, S. Forest, *et al.*, in *Cellular Metals and Metal Foaming Technology*, edited by J. Banhart, M.F. Ashby and N.A. Fleck (MIT Publishing, Berlin, 2003), pp. 301–306.
[14] L.J. Gibson and M.F. Ashby, *Cellular Solids. Structure and Properties*, 2nd edition, Cambridge Solid State Science Series (Cambridge University Press, Cambridge, 1997).
[15] H.N.G. Wadley, Adv. Engng Mater. **4** 726 (2002).
[16] X. Badiche, S. Forest, T. Guibert, *et al.*, Mater. Sci. Engng A **289** 276 (2000).
[17] J. Baruchel, J.-Y. Buffière, E. Maire, *et al.*, *X-Ray Tomography in Material Science* (Hermès, Paris, 2000).
[18] C. Berenstein, Contemp. Math. **278** 3 (2001).
[19] A. Faridani, K. Buglione, P. Huabsomboon, *et al.*, Contemp. Math. **278** 29 (2001).
[20] J.-Y. Buffière, E. Maire, P. Cloetens, *et al.*, Acta mater. **47** 1613 (1999).
[21] J. Serra, *Image Analysis and Mathematical Morphology*, vol. 2: *Theoretical Advances* (Academic Press, New York, 1988).
[22] C. Lantuéjoul and F. Maisonneuve, Pattern Recogn. **17** 177 (1984).
[23] F. Meyer and S. Beucher, J. Vis. Commun. Image Represent. **1** 21 (1990).
[24] J.A.F. Plateau, *Statique Expérimentale et Théorique des Liquides Soumis aux Seules Forces Moléculaires* (Gauthier-Villiard, Paris, 1873).
[25] P. Barma, M.B. Rhodes and R. Salovey, J. appl. Phys. **49** 4985 (1978).
[26] A. Fazekas, R. Dendievel, L. Salvo, *et al.*, Int. J. mech. Sci. **44** 2047 (2002).
[27] W.E. Lorensen and H.E. Clyne, Comput. Graph. **21** 163 (1987).
[28] G. Menges and F. Knipschild, Polym. Sci. Engng **15** 623 (1975).
[29] W. Thomson, Sir, Acta Math. **11** 121 (1887).
[30] E.B. Matzke, Am. J. Bot. **33** 58 (1945).

[31] D. Weaire and R. Phelan, Phil. Mag. Lett. **69** 107 (1994).
[32] C. Monnereau and M. Vignes-Adler, J. Colloid Interf. Sci. **202** 45 (1998).
[33] T. Aste, D. Boose and N. Rivier, Phys. Rev. E **53** 6181 (1996).
[34] R. Kusner and J.M. Sullivan, Forma **11** 233 (1996).
[35] D. Weaire and S. Hutzler, *The Physics of Foams* (Clarendon Press, Oxford, 1999).
[36] T. Dillard, Caractérisation et simulation numérique du comportement mécanique des mousses de nickel: morphologie tridimensionnelle, réponse élastoplastique et rupture. Thèse de doctorat, Ecole des Mines de Paris (2004).